Environmental Science and Ecotechnology 25 (2025) 100559

Contents lists available at ScienceDirect

Environmental Science and Ecotechnology

journal homepage: www.journals.elsevier.com/environmental-science-and-ecotechnology/

Original Research

MnO_2-Catalyzed electrocatalytic mineralization of triclosan in chlorinated wastewater

Asma Batool [a, b], Shan Shao [b], Kartick Chandra Majhi [b], Azeem Mushtaq [b], Yi Jiang [a, c], Wingkei Ho [a, d], Yiu Fai Tsang [a, d], Yuhe He [a, b], Kenneth Mei Yee Leung [a, e], Jason Chun-Ho Lam [a, b, *]

[a] State Key Laboratory of Marine Pollution, City University of Hong Kong, Kowloon Tong, Kowloon, Hong Kong Special Administrative Region of China
[b] School of Energy and Environment, City University of Hong Kong, Kowloon Tong, Kowloon, Hong Kong Special Administrative Region of China
[c] Department of Civil and Environmental Engineering, The Hong Kong Polytechnic University, Hung Hom, Kowloon, Hong Kong Special Administrative Region of China
[d] Department of Science and Environmental Studies, The Education University of Hong Kong, Tai Po, New Territories, Hong Kong Special Administrative Region of China
[e] Department of Chemistry, City University of Hong Kong, Kowloon Tong, Kowloon, Hong Kong Special Administrative Region of China

ARTICLE INFO

Article history:
Received 28 August 2024
Received in revised form
24 March 2025
Accepted 24 March 2025

Keywords:
Endocrine disruptors
Triclosan
Real wastewater
Synthetic and real landfill leachate
Mineralization
α-MnO_2-CC and δ-MnO_2-CC

ABSTRACT

The rising concentrations of xenobiotic aromatic compounds in the environment pose significant risks to human and ecosystem health. Developing a universal, environmentally benign, and scalable platform for mineralizing organic pollutants before their release into the environment is therefore crucial. Electrocatalysis can be highly advantageous for wastewater treatment because it is immediately responsive upon applying potential, requires no additional chemicals, and typically uses heterogeneous catalysts. However, achieving efficient electrochemical mineralization of wastewater pollutants at parts-per-million (ppm) levels remains a challenge. Here, we report the use of manganese dioxide (MnO_2), an Earth-abundant, chemically benign, and cost-effective electrocatalyst, to achieve over 99% mineralization of triclosan (TCS) and other halogenated phenols at ppm levels. Two highly active MnO_2 phases—α-MnO_2-CC and δ-MnO_2-CC—were fabricated on inexpensive carbon cloth (CC) support and evaluated for their ability to oxidatively degrade TCS in pH-neutral conditions, including simulated chlorinated wastewater, real wastewater, and both synthetic and real landfill leachates. Total organic carbon analysis confirmed the effective degradation of TCS. Electron paramagnetic resonance and ultraviolet−visible spectroscopy identified reactive oxygen species, enabling the construction of a detailed TCS degradation pathway. Upon optimization, the TCS removal rate reached 38.38 nmol min^{-1}, surpassing previously reported rates achieved with precious and toxic metal co-catalysts. These findings highlight MnO_2-CC as a promising, eco-friendly electrocatalyst with strong potential for upscaled remediation of organic pollutants in wastewater treatment.

1. Introduction

Industrial and anthropogenic activities generate large amounts of harmful organic waste that seriously threatens the environment and human health [1]. In particular, halogenated organic pollutants (HOPs) have high bioaccumulation potentials and are highly resistant to conventional biodegradation [2,3]. Thus, HOPs persist in the environment, where they can bioaccumulate and cause acute cytotoxicity in humans and other organisms [4]. For instance, triclosan (TCS) is a typical HOP widely used as an antiseptic and antimicrobial chemical in many quotidian goods, such as cosmetic, hygiene, and household cleaning products. It has been entering wastewater treatment plants (WWTPs) in a range of concentrations (0.00007−14 parts per million) for more than 30 years [5]. Over recent decades, various techniques, including physical methods

* Corresponding author. comment_hash{commentForInsertingAff}State Key Laboratory of Marine Pollution, City University of Hong Kong, Kowloon Tong, Kowloon, Hong Kong Special Administrative Region of China.
E-mail address: jason.lam@cityu.edu.hk (J.C.-H. Lam).

https://doi.org/10.1016/j.ese.2025.100559

(e.g., adsorption), oxidation processes (e.g., chlorination, photolysis/photocatalysis, ozonation, Fenton processes, and electrochemical oxidation), and biological approaches have been developed to treat triclosan-contaminated wastewater [6]. Among these, tertiary treatments, such as Fenton oxidation, electrolysis, piezo-electrocatalysis, and photocatalysis, have been extensively studied for degrading refractory contaminants in aqueous environments [7]. However, their applicability is often limited by factors such as low reaction rates, sludge stabilization and activation challenges, incomplete dehalogenation, and the high costs of stoichiometric reagents [7]. Although biodegradation and adsorption are cost-effective and environmentally friendly, they also face challenges, such as the generation of solid residues and the need for pre-treatment to convert pollutants into less toxic byproducts [8].

Primary treatment is estimated to remove approximately 28% of TCS from wastewater, while secondary and tertiary treatments can remove over 80% [9]. The TCS concentrations in WWTP influents and effluents worldwide are 0.0013–86.2 parts per million (ppm) and 0.0031–5.53 ppm, respectively, indicating that the complete removal of TCS from wastewater remains challenging [9].

Over the past decade, tertiary treatments, such as electrocatalytic treatments [10,11], have drawn increasing attention due to their unique ability to function immediately and robustly in ambient aqueous conditions. Moreover, several authors have reported using electrochemical or hybrid methods for TCS degradation (Table 1), and the TCS removal rates of these methods at ppm levels ranged from 5.77 to 28.8 nmol min^{-1}. Although all of these methods operate under ambient conditions, many require elaborated electrodes, such as boron-doped diamond (BDD) [12], or even toxic elements such as lead [13], to degrade TCS. Some hybrid methods do not need elaborated or toxic materials; for example, an electrocatalytic Fenton method had a high TCS removal rate (i.e., 43.25 nmol min^{-1}) [14]. However, it generated stoichiometric quantities of ferrous ions to facilitate the rapid degradation of TCS with hydrogen peroxide. Other advanced oxidation processes, such as photocatalytic and bio-chemical hybrid processes, have been applied for TCS degradation and exhibited reasonable TCS removal rates (i.e., 28.8 nmol min^{-1}) [14–16]. Nevertheless, these methods have several limitations or require specific conditions, such as costly electrodes, an organic cosolvent, or stoichiometric oxidants, thereby hindering their large-scale implementation. Therefore, there is a need to use Earth-abundant elements to fabricate active electrodes that can serve as an economical and feasible means of removing persistent TCS from wastewater.

Manganese oxide (MnO_2)-based electrocatalysts are highly promising, as they are inexpensive, chemically benign, and exhibit high catalytic activities [25–27]. MnO_2 can exist in different structural phases, namely the α-, β-, γ-, δ-, and λ-phases, which consist of the same octahedral MnO_6 units linked in different ways. Thus far, natural birnessite MnO_2 has been applied in slurries for the non-electrocatalytic oxidation of organic compounds, such as phenols [28], anilines [29], fluoroquinolones [30], and antibacterial amine-oxides [31]. The high structure–activity variability in MnO_2 presents an excellent opportunity to develop a cost-effective electrocatalyst to remove TCS from wastewater [32].

Herein, we report a novel hydrothermal exfoliation protocol to synthesize two different nano-MnO_2 structures, namely α-phase MnO_2 nanoneedles (NNs) and δ-phase nanosheet arrays (NSAs), which were anchored on a cost-effective carbon cloth (CC) support to form MnO_2 electrocatalysts. Both MnO_2 electrocatalysts mineralized TCS at ppm levels in chlorinated wastewater simulated as WWTP effluent [33] at room temperature under open-atmosphere conditions. Reactive oxygen species (ROS) were identified using electron paramagnetic resonance (EPR) and ultraviolet–visible (UV–vis) spectroscopy, and the mechanism of TCS degradation and the intermediates involved in substrate scope studies were

Table 1
Advanced oxidation methods to mineralize triclosan in aqueous environments.

Method	Concentration (ppm)	Removal rate (nmol min^{-1})	Degradation rate (%)	Conditions[a]	Catalyst	Co-catalyst/ Oxidant	Solvent
Electro. (this work)	10	38.38	100	Ambient	δ-MnO_2 on CC. 20 mA cm^{-2}	-	pH 7 DI water
Electro [17].	0.8	5.77	N.D.	Ambient (22 °C, dark)	First: Ti/MMO Second: Nb/BDD 2–14 mA cm^{-2}	-	pH 8 DI water
Electro [18].	3	830	99.9	Ambient	Ti/SnO_2–Sb/Ce-PbO_2 2 –10 mA cm^{-2}	400 ppm Ce^{3+}	pH 3–11 DI water
Electro [19].	5	28.8	98	Ambient	Ti/SnO_2–Sb/Gd-PbO_2 10 mA cm^{-2}	Gd^{3+}	pH 3 urine
Photo [15,20].	10	28.8	100	Ambient	Anatase and rutile TiO_2	-	pH 6.6 DI water
Fenton [16,21]	10	28.8	100	Ambient (20 –50 °C)	1 ppm Fe^{3+}	25 ppm H_2O_2	pH 3 HNO_3 and DI water
E.-Fenton [16]	50	[b]$k = 0.0128$ min^{-1}	91.39	Ambient	Fe:Mn-SBC 15 mA cm^{-2}	2600 ppm $KMnO_4$ 748 ppm Fe^{2+} 5.42 ppm H_2O_2	pH 3 real waste water
E.-Fenton [14,22]	10	43.25	99.9	Ambient	2:1 Fe:Mn-PC 10 mA cm^{-2}	-	pH 3 DI water
Fenton [23]	10	One: 14.41 (180 min) Two: 86.5 (30 min)	One: 82.7% (180 min) Two: 96.1% (30 min)	Ambient	500 ppm $BiFeO_3$ NPs	One: 10 mM H_2O_2 Two: 0.5 mM EDTA 10 mM H_2O_2	pH 6 DI water
Biochemical hybrid [24]	5	28.8	100	Anaerobic	1000 p.m. Pd/Fe NPs *Laccase* with syringaldehyde	-	pH 5.6–7.8 DI water

Note: Electro., Electrocatalytic; Photo., Photocatalytic; E.-Fenton, Electrocatalytic Fenton; Conc., Triclosan concentration; N.D., Not detected; BDD, Boron-doped diamond; MMO, Mixed metal oxides; SBC, Sludge-based carbon; CB, Carbon black; PC, Porous carbon; NPs, Nanoparticles; EDTA, Ethylenediaminetetraacetic acid; DI water, Deionized water; *k*, rate constant.

[a] Unless specified otherwise, "ambient" refers to the conditions of 25 °C and 1 atm.

[b] Volume data were not available.

elucidated using gas chromatography–mass spectrometry. Total organic carbon (TOC) analyses were performed to confirm TCS mineralization.

2. Materials and methods

2.1. Materials

All chemicals were used as received. Potassium permanganate ($KMnO_4$), ammonium sulfate $(NH_4)_2SO_4$, manganese sulfate monohydrate ($MnSO_4 \cdot H_2O$), and 2-bromophenol (2-BrPh) were obtained from Macklin (Shanghai, China). 4-Chlorophenol (4-CP), bisphenol A (BPA), and triclosan (TCS) were obtained from the Tokyo Chemical Industry (Tokyo, Japan). 2,4,6-Trichlorophenol (2,4,6-TCP) was obtained from Thermo Scientific (Waltham, United States). Methanol (High-performance Liquid Chromatography grade), acetone, and ethanol (Analytical grade) were used. Sodium sulfate (Na_2SO_4) and sodium chloride (NaCl) were obtained from Fisher (Pittsburgh, United States).

2.2. Fabrication of MnO_2 nanostructures on a carbon cloth support

MnO_2 nanostructures were fabricated on CC via hydrothermal exfoliation (Fig. 1a). First, the CC was sonicated successively in acetone, ethanol, and deionized water to remove adsorbed impurities. For α-phase MnO_2 preparation, the sonicated CC (1 cm × 3 cm) was hung on the walls of a Teflon-lined autoclave while immersed in 40 mL of an aqueous solution of 220 mg $KMnO_4$ and 60 mg $MnSO_4 \cdot H_2O$. Next, the autoclave was sealed, heated at 140 °C for 20 h, and cooled to room temperature overnight. As a result, a thin film of α-MnO_2 was deposited on the CC, with some residual powder left at the autoclave bottom. δ-phase MnO_2 (δ-MnO_2) was prepared on CC under similar hydrothermal conditions but with different precursors and heat treatment. Here, the hanging sonicated CC was immersed in 40 mL of a solution containing 126.4 mg $KMnO_4$ and 42.8 mg $(NH_4)_2SO_4$ and heated at 110 °C for 20 h.

All MnO_2 electrodes were annealed at 350 °C for 2 h at a heating rate of 10 °C min^{-1}. The respective electrodes were denoted as α- and δ-MnO_2-CC. The electrodes were stored at room temperature until use. The residual dark brown (α-MnO_2) and black (δ-MnO_2) precipitates from the autoclaves were also collected and stored under similar conditions for further characterization.

2.3. Electrocatalytic oxidation experiments and product analysis

All electrolysis experiments were conducted in an undivided batch reactor (100 mL) containing a MnO_2 anodic working electrode (geometric area = 1 cm^2) and nickel foam as a cathodic counter electrode. All solutions contained 10 ppm of endocrine disruptors (EDCs) and were prepared in aqueous media containing 50 mM Na_2SO_4 and 5 mM NaCl to provide background ionic strength and mimic the salinity of natural wastewater effluent [34]. Chronopotentiometric electrolysis was performed at 20, 40, and 80 mA cm^{-2} at room temperature (23 ± 2 °C). Aliquots of samples were collected periodically and analyzed using a high-performance liquid chromatography (HPLC, Agilent 1260 Infinity II) equipped with a photodiode array detector and a reverse-phase Zorbax XDB-C18 column (3.9 × 150 mm), which was eluted isocratically with a methanol:water (70:30, v/v%) mobile phase at a flow rate of 1 mL min^{-1}. The intermediate products were detected using a gas chromatograph (GCMS, Shimadzu 2010 Ultra Gas Chromatograph–Mass Spectrometer) equipped with a capillary column (Agilent DB-5, 30 m × 0.25 mm internal diameter × 0.25 μm) in splitless mode at an injection temperature of 200 °C. All samples subjected to gas chromatography analysis (100 mL each) were extracted with 4 mL of dichloromethane, followed by drying with anhydrous Na_2SO_4. Gas chromatograms were analyzed by comparison with the National Institute of Standards and Technology library and external references to identify intermediates. The extent of mineralization was determined by TOC analysis (Shimadzu, TOC-L_{CPH}).

2.4. Structural phase and morphology analysis

The crystallinity and phase structure of the MnO_2 electrodes and residual powders were determined by X-ray diffraction (PANalytical X'Pert X-ray diffractometer) using copper Kα radiation (40 kV, 30 mA). The qualitative and quantitative surface properties of the prepared electrodes were evaluated by high-resolution scanning electron microscopy *(FEI–Philips XL30 Esem-FEG)*. Raman spectroscopy was performed using a Raman spectrometer (EnSpectr R532, EnSpectr) equipped with a 20 mW, 532 nm laser. X-ray photoelectron spectroscopy (XPS) was performed on a Thermo Kα photoelectron spectrometer, and monoenergetic aluminum Kα radiation was employed to characterize and quantify the distribution of the phases. All electrochemical experiments, i.e., linear sweep voltammetry (LSV) and cyclic voltammetry (CV), were conducted in a three-electrode setup using a CHI 660 E electrochemical station (CH Instruments, Inc., Shanghai) in 15 mL of 1 M Na_2SO_4 electrolyte under ambient conditions. Unless specified otherwise, a standard bulk electrolysis reaction involved an as-prepared MnO_2 electrode as the working electrode (area = 1 cm^2); a Nickel mesh and a 3.5 M silver/silver chloride (Ag/AgCl) electrode were used as the counter and reference electrode, respectively.

2.4.1. Measurement of the electrochemical active surface areas of uncoated and MnO_2-Coated electrodes

The electrochemical active surface areas (ECSAs) of the electrodes were calculated from the electrochemical double-layer capacitance (C_{dl}) of the catalytic surface obtained from double-layer charging curves, which were determined by CV at 0–0.8 V (a non-Faradaic region) at a scan rate of 20–200 mV s^{-1} with an interval of 20 mV s^{-1}. Specifically, C_{dl} was measured from the slope of the j–ν curve, where j is the non-Faradaic capacitive current obtained from a CV curve, and ν is the scan rate. Next, the *ECSA* was calculated using the following equation: $ECSA = C_{dl}/C_s$, where C_s is the specific capacitance set to 0.02 mF cm^{-2} as previously published [35].

3. Results and discussion

3.1. Structural analysis of α- and δ-MnO_2 nanostructures

The nanostructures and morphologies of the MnO_2 electrodes were examined using scanning electron microscopy (SEM). The bare CC had a smooth fibrous morphology (Fig. 1b). The α- and δ-MnO_2 electrodes uniformly covered the CC surface. The α-MnO_2-CC exhibited interconnected NNs on the CC surface, with an estimated thickness of 200–300 nm (Fig. 1c). The δ-MnO_2-CC exhibited interconnected NSAs that formed a micron-sized sea-urchin-like morphology (Fig. 1d). These ordered NSAs formed an open-network-like structure (Supplementary Material Fig. S1a), and the average thickness of a single nanosheet was estimated to be 22.5 nm (Supplementary Material Fig. S1b).

Energy-dispersive X-ray spectrometry (EDS) mapping analysis was performed to quantify elemental Mn, O, and C content. The Mn content (Fig. 1e) illustrates the relatively uniform Mn distribution on the surface of the MnO_2 electrodes. Strong Mn and O signals were observed (Supplementary Material Fig. S2) in both phases of

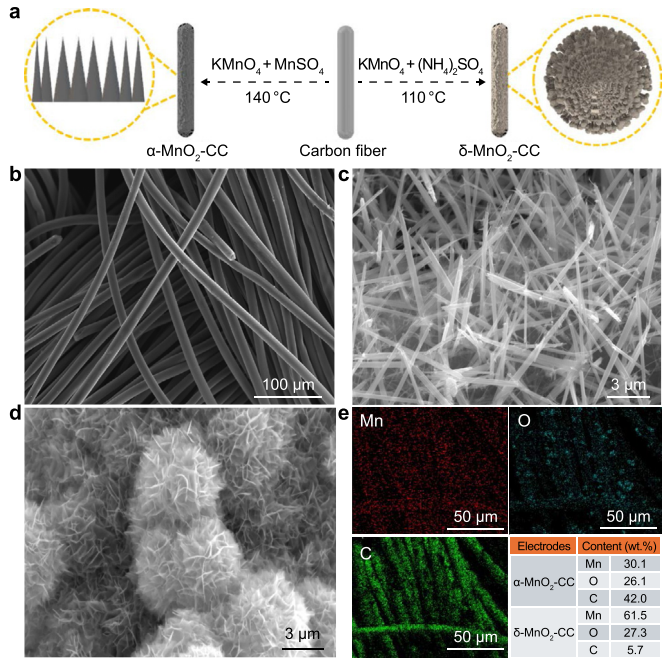

Fig. 1. **a**, Schematic illustration of the fabrication of MnO_2 nanostructures on a carbon cloth (CC) surface. **b**–**d**, Scanning electron microscopy images of bare CC (**b**), α-MnO_2-CC (**c**), and δ-MnO_2-CC (**d**). **e**, Energy-dispersive X-ray spectroscopy elemental mapping images of MnO_2 on the CC surface.

MnO_2-CC, and the intensity was doubled on the δ-MnO_2-CC (61.54 wt%, Supplementary Material Fig. S2b) compared with α-MnO_2-CC (30.06 wt%, Supplementary Material Fig. S2a). In addition, the exposed carbon content of δ-MnO_2-CC (5.72 wt%) was much less than that of α-MnO_2-CC (42.02 wt%), indicating greater coverage of the CC surface on δ-MnO_2-CC than on α-MnO_2-CC (Supplementary Material Table S1).

X-ray diffractometry (XRD) was performed to examine the crystallinity of the MnO_2 electrodes. The XRD patterns of bare CC and of α-phase MnO_2 NNs and δ-phase MnO_2 NSAs on CC are shown in Fig. 2a. Two XRD peaks at 26° and 43° were observed on the bare CC surface, consistent with the literature [36]. Neither α-MnO_2 nor δ-MnO_2 exhibited well-defined peaks, indicating that they had amorphous structures. Nevertheless, the α-MnO_2 peaks and the δ-MnO_2 peaks agree with Powder Diffraction File card #44–0141 and Joint Committee on Powder Diffraction Standards card #18–802, respectively [37]. The differences between the phase structures of the synthesized forms of MnO_2 were confirmed by their peak patterns. Also, α-MnO_2-CC had a predominant (211) plane of Mn, as shown by its narrow, high-intensity peaks. In contrast, δ-MnO_2-CC demonstrated broader and weaker (411) and (521) peaks at 38° and 50°, respectively. The XRD patterns of residual MnO_2 powders collected from the autoclave following the synthesis of α- and δ-MnO_2 were also analyzed to determine their crystal phases (Supplementary Material Fig. S3). Their XRD patterns were consistent with those of MnO_2 deposited on the CC surface.

Raman spectroscopy of MnO_2-CC electrodes was performed using a Raman spectrometer equipped with a 20 mW, 532 nm laser. Raman spectroscopy (Fig. 2b) confirmed the clear difference between two versions of MnO_2. δ-MnO_2 had been formed, as the Raman spectrum contained representative peaks at 160.4, 504.6, 581.8, and 654.6 cm^{-1}, which are consistent with the literature [38]. The X-ray photoelectron spectra of α-MnO_2-CC and δ-MnO_2-CC are shown in Fig. 2c–f. Two peaks, centered on 642.4 and 654 eV representing the spin-orbit doublet states of Mn $2p_{3/2}$ and Mn $2p_{1/2}$, respectively, were present in the high-resolution spectrum of Mn 2p. After spectral decomposition, Mn existed in three valences: +2, +3, and +4. Both α- and δ-MnO_2 showed strong Mn^{3+} peaks at 642 and 654 eV for Mn $2p_{3/2}$ and Mn $2p_{1/2}$, respectively. Fig. 2d and f show the O 1s core-level spectra of α-MnO_2-CC and δ-MnO_2-CC, respectively. In addition to the dominant Mn–O–Mn moieties in MnO_2, represented by the peak at approximately 528.8 eV, there were large proportions of Mn–O–H moieties (i.e., Mn ions bonded with hydroxyl groups) and H–O–H moieties (i.e., absorbed water), represented by peaks at approximately 531.9 and 533.4 eV, respectively. The relative surface proportions of Mn^{3+} and Mn^{4+} ($Mn^{3+/4+}$) are often considered the main factors in the performance of Mn catalysts. For instance, a large proportion of Mn^{3+} on the surfaces of bifunctional catalysts has been found to facilitate the oxygen evolution reaction (OER) [39–42]. Conversely, a small proportion of Mn^{4+} on the surfaces of bifunctional catalysts has been suggested to enhance their adsorption of organic compounds [43]. The $Mn^{3+/4+}$ values for α-MnO_2-CC and δ-MnO_2-CC were 2.7079 and 1.6000, respectively, which matched well with the catalytic findings.

3.2. Determination of the ECSAs of the MnO_2 electrodes

The electrochemical characterization of the MnO_2 electrodes was conducted in a three-electrode batch system. Their ECSAs were

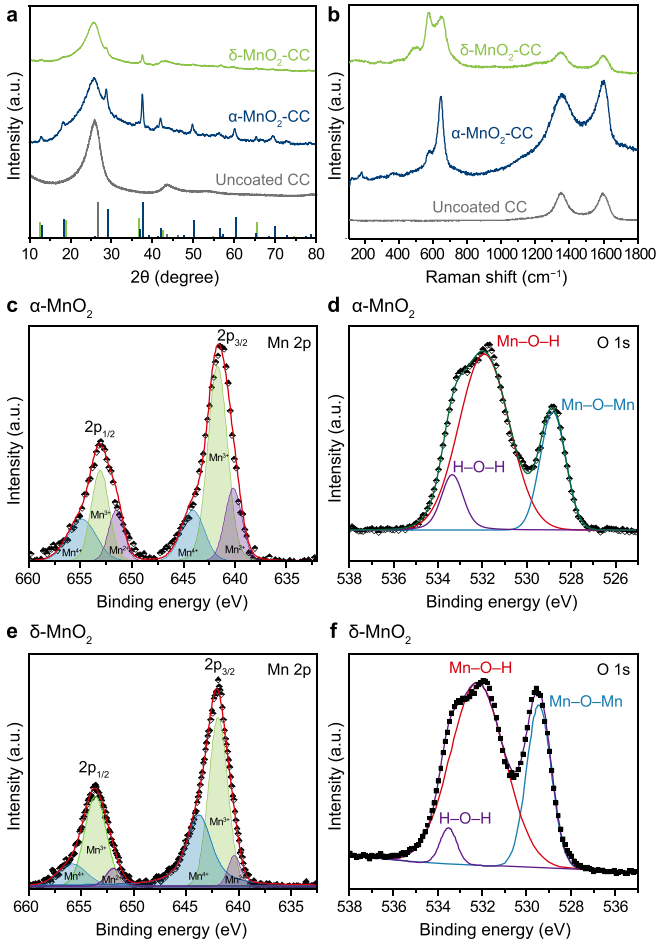

Fig. 2. **a**–**b**, X-ray diffraction patterns (**a**) and Raman spectra (**b**) of uncoated carbon cloth (CC), α-MnO_2-CC, and δ-MnO_2-CC. **c**–**f**, High-resolution X-ray photoelectron spectra of Mn 2p (**c**, **e**) and O 1s (**d**, **f**), together with the corresponding spectral decomposition of α-MnO_2-CC (**c**–**d**) and δ-MnO_2-CC (**e**–**f**).

determined via CV at 0–0.8 V in the non-Faradaic current region at a range of scan rates, i.e., 20–200 mV s^{-1}, with data collected every 20 mV. Fig. 3 shows the cyclic voltammograms of MnO_2-modified and uncoated electrodes measured in 1 M Na_2SO_4 solution. C_{dl} was determined by plotting the scan rate versus the change in current density ($\Delta J = J_{anodic} - J_{cathodic}$), as the resulting linear slopes equal $2C_{dl}$. The ECSAs of the α-MnO_2 electrode (Fig. 3a, inset) and δ-MnO_2 electrode (Fig. 3b, inset) were 33 and 62 times higher, respectively, than that of the CC electrode (Fig. 3c, inset). Moreover, the surface area of the δ-MnO_2 electrode was twice that of the α-MnO_2 electrode, which accounts for the effectiveness of the δ-MnO_2 electrode in degrading small aromatics, as described in Section 3.5.

3.3. Electrocatalytic TCS-degradation performance of α- and δ-MnO_2 electrodes

The electrocatalytic performance of the as-prepared α- and δ-MnO_2 in the oxidative degradation of TCS was evaluated via chronopotentiometric electrolysis in an aqueous environment containing 5 mM NaCl and 50 mM Na_2SO_4 at room temperature and atmospheric pressure. NaCl was added to provide conductivity and to mimic the typical chloride-ion concentration of wastewater [34]. The oxidative degradation of TCS by α- and δ-MnO_2 decreased as the current increased (Fig. 4a), indicating that the degradation efficiency was compromised by the increasing competitiveness of the OER driven by anodic water splitting. At 20 mA cm^{-2}, the proportion of TCS degraded by α- and δ-MnO_2 reached 97.27 ± 2.7% and 99.44 ± 1.4%, respectively, but at 40 mA cm^{-2}, this decreased to 85.18 ± 5.7% and 88.92 ± 5.5%, respectively. This result indicates that, compared with δ-MnO_2, α-MnO_2 was more affected by the OER. At 80 mA cm^{-2}, the proportion of TCS degraded by α-MnO_2 was only 63.27 ± 7.3%, whereas that degraded by δ-MnO_2 remained reasonably high: 82.58 ± 3.1%.

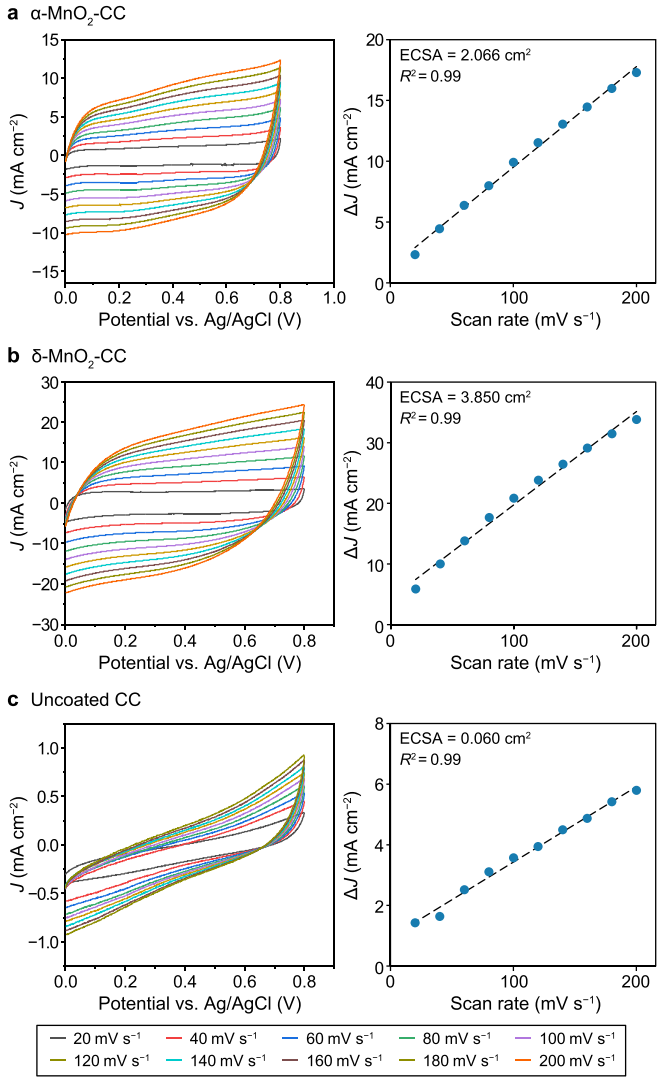

Fig. 3. Cyclic voltammetry curves of α-MnO_2-CC (**a**),δ-MnO_2-CC (**b**), and uncoated CC electrodes (**c**) in the non-Faradaic region of 0–0.8 V vs. Ag/AgCl, recorded at scan rates ranging from 20 to 200 mV s^{-1}. The subpanels on the right side of panels **a**–**c** display the corresponding electrochemical double-layer capacitance (C_{dl}) plots derived from the cyclic voltammetry curves. CC: carbon cloth.

The greater tendency of α-MnO_2 than δ-MnO_2 to exhibit the OER at high currents is consistent with a previous electrochemical observation that the α phase has a lower overpotential for OER than the δ phase; this implies that α-MnO_2 will trigger OER before δ-MnO_2 [44]. The OER activity of α-MnO_2 is superior to that of δ-MnO_2 because the former has a greater $Mn^{3+/4+}$ ratio on its surface, as demonstrated by XPS (Fig. 2c). Mn^{3+} favors the occurrence of the OER because the single electron occupying its σ*-orbital (eg) is transferred to its O–O π*-orbital when Mn^{3+} is oxidized to Mn^{4+} [45]. The model supports our XPS-based analysis of the surface, which revealed that $Mn^{3+/4+}$ ratios for the α- and δ-phases were 2.7079 and 1.6000, respectively (Fig. 2c–e). Thus, compared with the δ-MnO_2 catalyst, the α-MnO_2 catalyst had a larger proportion of Mn^{3+}, which shifted its activity from TCS degradation toward the OER.

In addition to δ-MnO_2 having a wider electrochemical window for the OER than α-MnO_2, δ-MnO_2 adsorbed more TCS (Supplementary Material Fig. S4). Specifically, in an open-circuit TCS adsorption control experiment, δ-MnO_2 absorbed 13.7% of the TCS to which it was exposed, whereas α-MnO_2 adsorbed only 8.3%. This is attributable to the ECSA of δ-MnO_2 being greater than that of α-MnO_2 (3.847 cm^2 versus 2.066 cm^2; Fig. 3a and b, panels on the right). Moreover, the electrocatalytic performance of as-synthesized MnO_2 electrodes for some mono- and di-aromatic structures were tested under the same conditions (Fig. 4b).

During the bulk electrolysis of TCS, trace amounts of chlorinated mono-aromatic intermediates were detected. Therefore, to elucidate the degradation pathways and obtain comprehensive mechanistic insights, TCS and the chlorinated mono-aromatics 4-CP and 2,4,6-TCP were subjected to time-resolved electrolysis on α-MnO_2 and δ-MnO_2 to investigate the relative rates of degradation by each catalyst. Two additional EDCs structurally similar to TCS were also examined under these conditions, namely BPA, due to its di-aromatic structure, and 2-BrPh, due to its halogenated structure (Fig. 4c and d). All electrolysis was performed at 20 mA cm^{-2} to minimize the possibility of competition with the OER. A pseudo-first-order kinetic analysis was conducted to calculate the degradation rate constants (k, min^{-1}; Fig. 4c and d, insets).

Under the initial conditions (j = 20 mA cm^{-2}), α-MnO_2 performed slightly better than δ-MnO_2, as all of the k values of the former were greater than those of the latter. All degradation patterns obeyed the pseudo-first-order kinetic model, as the data exhibited a good fit, i.e., the average coefficients of determination were 0.88 and 0.93 for the α-MnO_2 and δ-MnO_2 datasets, respectively, in linear regression using $\ln(C/C_0) = -kt$. The k of TCS degradation was 22 min^{-1} on α-MnO_2 and 9.6 min^{-1} on δ-MnO_2. α-MnO_2 also degraded BPA at a greater rate than did δ-MnO_2, indicating the universal applicability of α-MnO_2. Halogenated aromatic species that appeared during TCS degradation were also examined. 2,4,6-TCP was degraded by both α-MnO_2 (k = 16.4 min^{-1}) and δ-MnO_2 (k = 6.6 min^{-1}), with its degradation by the former being

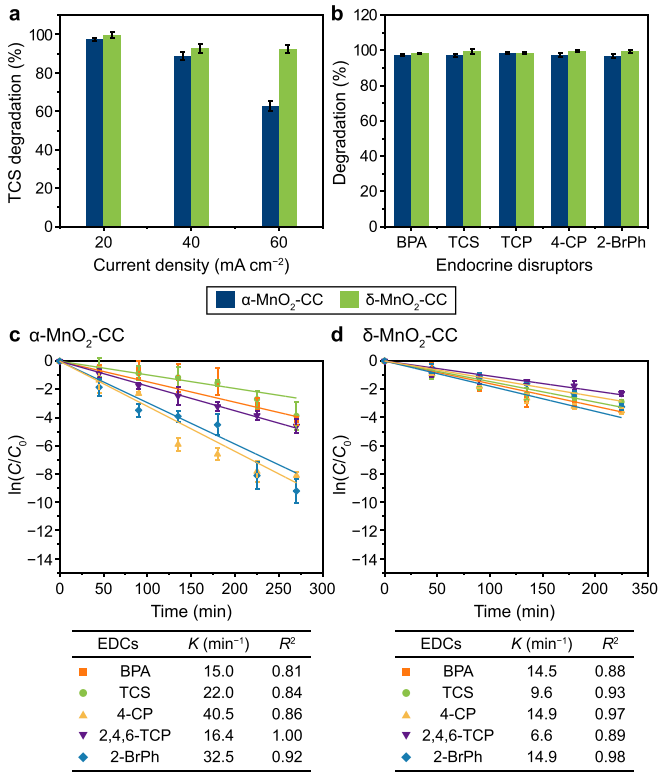

EDCs	K (min^{-1})	R^2
BPA	15.0	0.81
TCS	22.0	0.84
4-CP	40.5	0.86
2,4,6-TCP	16.4	1.00
2-BrPh	32.5	0.92

EDCs	K (min^{-1})	R^2
BPA	14.5	0.88
TCS	9.6	0.93
4-CP	14.9	0.97
2,4,6-TCP	6.6	0.89
2-BrPh	14.9	0.98

Fig. 4. a, Triclosan (TCS) degradation efficiencies of α-MnO_2-CC and δ-MnO_2-CC at different current densities. **b**, Electrocatalytic oxidative activity of α- and δ-MnO_2-CC for endocrine disruptors (EDCs, 10 ppm) at room temperature (25 °C) at 20 mA (4.5 h). **c**–**d**, Plots of ln(C/C_0) versus time indicating the first-order behavior of α-MnO_2-CC (**c**) and δ-MnO_2-CC (**d**) at a current density of 20 mA (where $C = C_t$ and $C_0 = C_i$). The tables below show the corresponding first-order parameters for TCS and related EDCs. The average of triplicate data and standard deviation is given in Supplementary Materials Tables S3–S6. CC: carbon cloth; EDC: endocrine disruptors; BPA: bisphenol A; TCP: trichlorophenol; 4-CP: 4-chlorophenol; 2-BrPh: 2-bromophenol.

slightly more efficient than its degradation by the latter. However, the rate constant for 4-CP degradation by α-MnO_2 (k = 40.5 min^{-1}) was almost thrice that for 4-CP degradation by δ-MnO_2 (k = 14.9 min^{-1}). We performed a control comparison using 2-BrPh and observed a similar rate enhancement for α-MnO_2 over δ-MnO_2 (k = 32.5 min^{-1} versus 14.9 min^{-1}), which indicated that the rapid degradation observed on α-MnO_2 was not due to the chlorine substituent of 4-CP but rather its monomeric ring structure and mono-halogenation. Control experiments (Fig. 4c and d) on open-circuit adsorption showed that α-MnO_2 and δ-MnO_2 had similar adsorption capacities (Supplementary Material Fig. S4) for 4-CP and 2,4,6-TCP, which indicated that the superior catalytic activity of α-MnO_2 was attributable to its intrinsic properties, i.e., the fact that it had a greater $Mn^{3+/4+}$ ratio (2.7079) than δ-MnO_2 (1.6000).

Overall, the degradation trend for α-MnO_2 was approximately 4-CP, 2-BrPh >2,4,6-TCP, TCS > BPA. The exceedingly high degradation of 2-BrPh and 4-CP by α-MnO_2 indicates that it excels at degrading halogenated mono-aromatics and does not appear to be restricted by the location of the halogen. An open-circuit adsorption control experiment was also performed using 4-CP and 2-BrPh and both α-MnO_2 and δ-MnO_2 catalysts. The results showed that δ-MnO_2 was slightly more effective than α-MnO_2 at adsorbing organic compounds, which excluded the possibility that favorable adsorption accounted for the high reactivity of α-MnO_2. Thus, we attribute the better performance of α-MnO_2 to the fact that it has a greater $Mn^{3+/4+}$ ratio than δ-MnO_2, which enhances the oxidative catalytic performance of α-MnO_2. The degradation trend for δ-MnO_2 was approximately 4-CP, 2-BrPh > BPA, TCS >2,4,6-TCP. This suggests that the accessibility of C–H sites on the aromatic ring of an EDC plays a key role in its oxidative degradation by δ-MnO_2. Specifically, 4-CP and 2BrPh have four accessible aryl C–H sites at which oxidation can occur; BPA and TCS also have four such sites per ring, but these sites may be sterically hindered by the molecules' bulky biphenyl structure; and 2,4,6-TCP only has two accessible aryl C–H sites.

XRD analysis was conducted on all the MnO_2 catalysts after electrolysis, and the results showed that they exhibited good retention of their respective phases (Supplementary Material Fig. S5). Thus, the α-MnO_2 peaks at 28.74° and 37.58° and the key δ-MnO_2 peak at 38.3° retained suitable shapes after exposure to all the EDC substrates.

3.4. Generation mechanism and role of ROS

EPR and UV–vis spectroscopy were used to identify the ROS. The following text describes a possible mechanism based on the spectroscopic results. First, the anodic oxidation of two chloride ions (Cl^-) affords molecular chlorine (equation (1)) [46], which then combines with H_2O to yield hypochlorous acid (HClO; equation (2)) [47]. The presence of HClO was confirmed by UV–vis spectroscopy, as it showed an increase in the size of the peak at ~290 nm, which matches the reported wavelength of HClO in UV–vis spectra (Fig. 5g and h). Next, HClO reacts with either a chlorine radical ($Cl^•$; equation (3)) [48] or a hydroxyl radical ($HO^•$; equation (4)) [49] to yield chlorine monoxide ($ClO^•$), which subsequently reacts with a hydroxide ion to afford a superoxide anion ($O_2^{•-}$; equation (5)) [50]. Studies have suggested that $ClO^•$ can react with $HO^•$ to yield a chlorite ion [51], which is commonly used as an oxidizing agent. It can accept electrons from other substances, leading to the formation of chloride ions and chlorine dioxide.

To confirm the formation of chlorite ions in our reaction medium, we examined the reaction using spin-trap-free EPR spectroscopy, and the results showed that the reaction did not follow such a pathway (Fig. 5c–f). Specifically, the EPR spectrum of the reaction electrolyte (which contained both Na_2SO_4 and NaCl) contained no signals for $HO^•$ because this species had been scavenged by Cl^- [46] and the increasing amount of HClO (equation (4)). We separately examined the reaction using Cl^--free EPR spectroscopy, which confirmed that $HO^•$ could be formed by both MnO_2 electrodes (Fig. 5b–e). The presence of $O_2^{•-}$ was also confirmed by EPR spectroscopy, which showed that the splitting pattern corresponded to 5,5-dimethyl-1-pyrroline *N*-oxide–superoxide with a hyperfine coupling constant of 14.4, which is consistent with the published value of 14.53 [52,53] (Fig. 5a). Finally, the reaction of HClO with $O_2^{•-}$ forms additional $HO^•$ and Cl^-, which are subsequently converted to various reactive chlorine species (RCS), such as $ClO^•$ and $Cl^•$ (equation (6)) [46–49,51,54,54].

$$2Cl^- \rightarrow 2Cl_2 + 2e^- \quad (1)$$

$$Cl_2 + H_2O \rightarrow HClO + HCl \quad (2)$$

$$HClO + Cl^• \rightarrow ClO^• + H^+ + Cl^- \quad (3)$$

$$HClO + HO^• \rightarrow ClO^• + H_2O \quad (4)$$

$$ClO^• + OH^- \rightarrow O_2^{•-} + H^+ + Cl^- \quad (5)$$

$$HClO + O_2^{•-} \rightarrow HO^• + Cl^- \rightarrow RCS \quad (6)$$

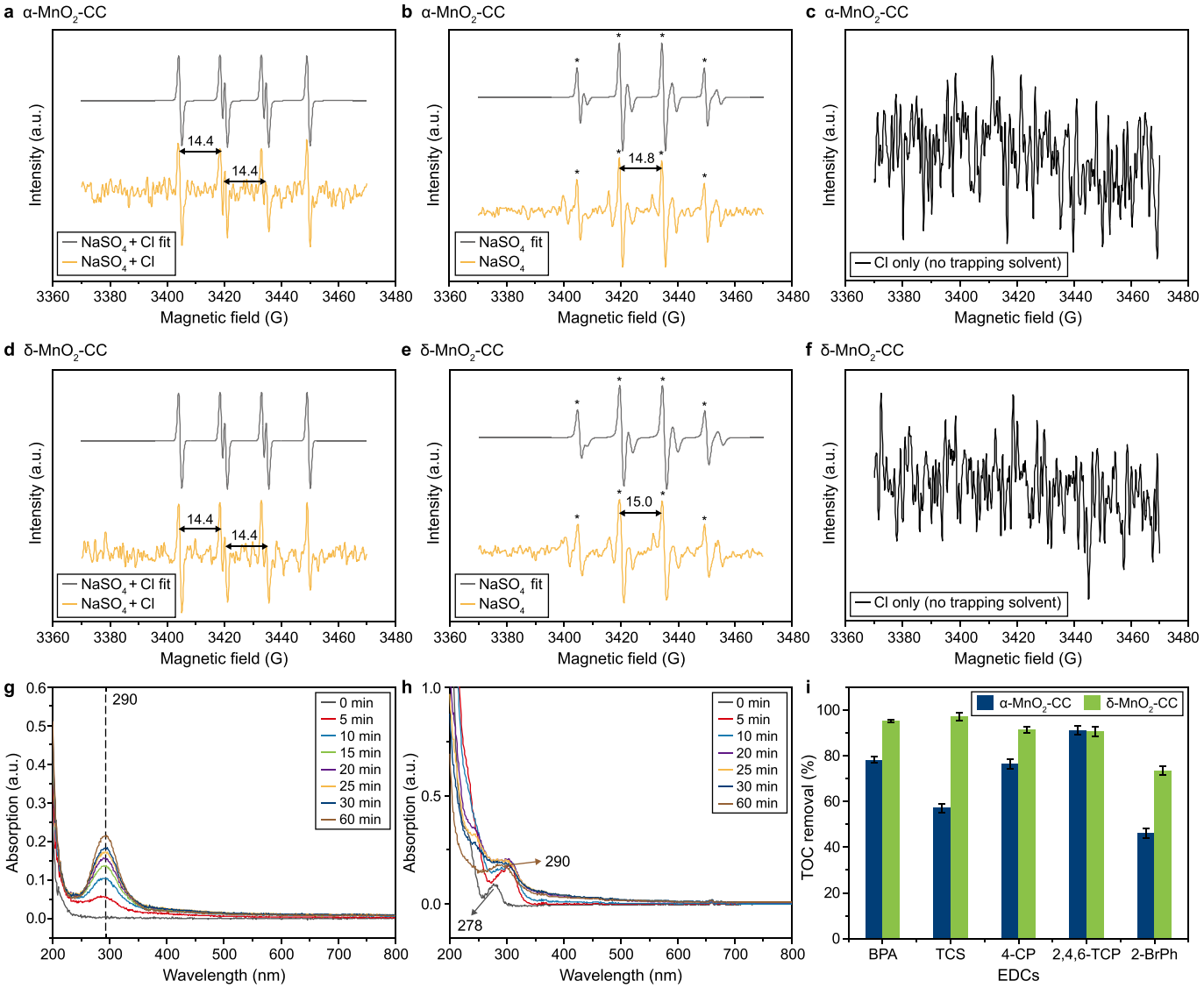

Fig. 5. **a**–**f**, Electron paramagnetic resonance analysis of electrochemical oxidative mineralization of triclosan (TCS) by MnO_2 electrocatalysts [α-MnO_2-CC (**a**–**c**) and δ-MnO_2-CC (**d**–**f**)] in different electrolytes: Na_2SO_4 + Cl (**a**, **d**); Na_2SO_4 (**b**, **e**); and Cl environment only (**c**, **f**). **g**–**h**, Formation of hypochlorous acid in the absence (**g**) and presence (**h**) of TCS. **i**, Total organic carbon removal by the electrochemical oxidative mineralization of TCS and structurally similar EDCs by the MnO_2 catalysts. The average triplicate data and the standard deviation are given in Supplementary Material Table S7. CC: carbon cloth; EDCs: endocrine disruptors; BPA: bisphenol A; TCP: trichlorophenol; 4-CP: 4-chlorophenol; 2-BrPh: 2-bromophenol; *: corresponds to hydroxy radical signal.

Based on the spectroscopic analysis, HClO appears to be the ROS responsible for the degradation of TCS. In the presence of TCS, a slight redshift of the λ_{max} from ~290 to 304 nm indicated the consumption of HClO by TCS. After the complete mineralization/disappearance of TCS, the λ_{max} returned to ~290 nm, indicating the reformation of HClO. In the absence of Cl^-, however, $HO^\bullet$ was the dominant ROS (Fig. 5b–e), as HClO could not form, and the degradation of TCS was significantly slower (Supplementary Material Fig. S6). This demonstrated that $HO^\bullet$ could not degrade TCS efficiently.

TOC was measured to quantify the extent of organic content mineralization resulting from oxidative degradation (Fig. 5i). Before measuring TOC content after the degradation of EDCs, TOC content after electrolysis of both MnO_2 electrodes without compounds were measured as a control experiment (Supplementary Material Table S2). The δ-MnO_2 degraded TCS and its structurally similar EDCs very efficiently. Over 90% of TOC was removed after electrochemical treatment of TCS, BPA, and halogenated phenols. In comparison, α-MnO_2 was less efficient at complete mineralization because as the TOC decreased, the electrochemical oxidative degradation of organics occurred via the OER rather than by mineralization. Meanwhile, although the catalytic performance of δ-MnO_2 was less active, it was less prone to exhibit the OER and thus achieved better mineralization. Only 2,4,6-TCP underwent more than 90% degradation on both α- and δ-MnO_2 catalysts, which indicates that such highly chlorinated species can be degraded effectively by these catalysts, regardless of the nature of their surfaces.

3.5. TCS mineralization pathway and toxicity evaluation

Fig. 6 and S8 (Supplementary Material) depict a possible TCS-degradation pathway based on the literature findings and products detectable by mass spectrometry [55,56]. The observed

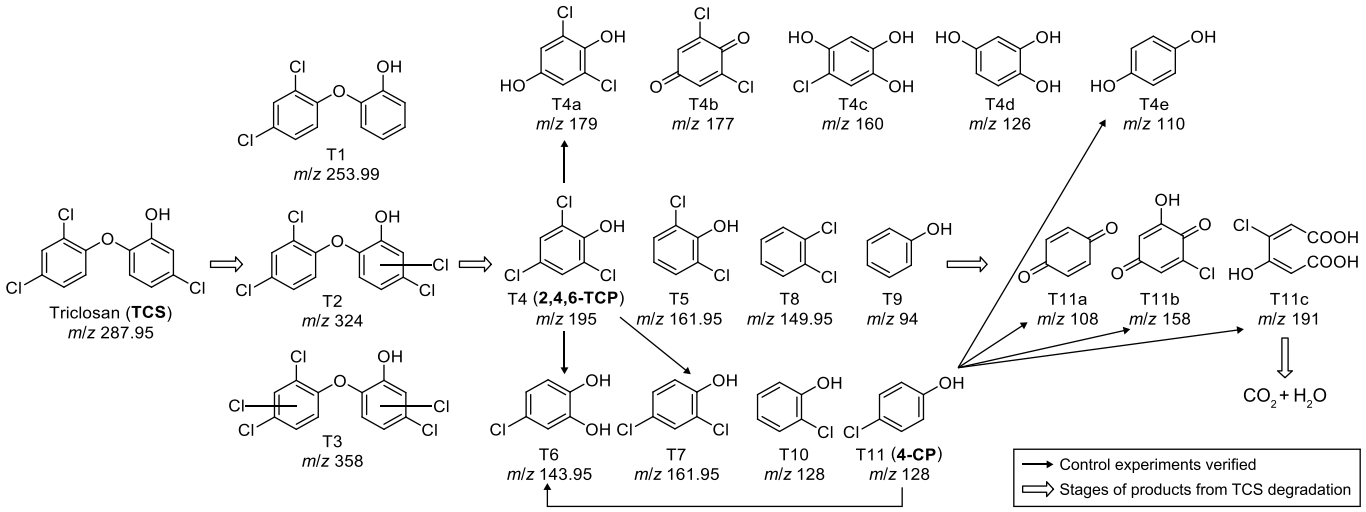

Fig. 6. Possible pathway of electrochemical oxidative mineralization of triclosan in an aqueous environment based on products that can be observed by mass spectrometry.

fragments were categorized based on their structural complexity and appearance during electrolysis.

Based on the detectable fragments, we propose that TCS initially undergoes chlorination and dichlorination to form T1 (*m/z* 253.99), T2 (*m/z* 324), and T3 (*m/z* 358). Subsequently, cleavage of the aryl ether C–O bond produces various mono-aromatic products: T4 (2,4,6-TCP, *m/z* 195), T5 (*m/z* 161.95), T6 (*m/z* 143.95), T7 (*m/z* 161.95), T8 (*m/z* 149.95), T9 (*m/z* 94), T10 (*m/z* 108), and T11 (4-CP, *m/z* 128).

Further, we conducted two control experiments to confirm the ring-opening pathway of transformation products. First, a control experiment was conducted to electrolyze T4 (2,4,6-TCP) separately to determine whether multi-chlorinated aromatic monomers are degradable under our conditions. The reaction produced T4a (*m/z* 179), T6, and T7. As T6 and T7 were also formed during TCS electrolysis, this confirmed that T4 underwent degradation during the TCS degradation trials. We propose that the electrode oxidizes T4–11 to yield T11a (*m/z* 108), T11b (*m/z* 158), and T11c (*m/z* 191). Although T11a–c were not observed directly during TCS electrolysis, we posit that they are formed during TCS degradation because the oxidative treatment of mono-aromatics is known to yield quinones and ring-opened carboxylic acids [33]. We thus conducted a second control experiment in which we electrolyzed T11 (4-CP) under the same conditions and obtained detectable amounts of T11a–c. The absence of T11a–c during TCS degradation is attributable to the fact that only low concentrations of T11 were formed. We hypothesize that T11a–c is oxidized and mineralized to carbon dioxide and H_2O. The cleavage of dimers occurred at the ether C–O bonds, but this cleavage occurred non-selectively on either side. Chlorination also occurred, confirming that RCS were formed during electrolysis (equation (6)). Nevertheless, the mineralization of aromatic compounds continued, as confirmed by the TOC analysis. After electrochemical treatment, the amount of organic carbon substantially decreased. Small amounts of a hydroxylated product (i.e., T6) were observed during the TCS degradation and the control T4 trials, which confirmed that HO• had been formed (equation (6)).

The acute and chronic toxicity of TCS and its individual transformation product on fish and daphnids is predicted by the Ecological Structure Activity Relationships (ECOSAR) software (Supplementary Material Table S10). The tabulated dataset provides a comprehensive overview of TCS and its transformation products, detailing their chemical structures through simplified molecular input line entry system (SMILES), molecular weights (*m/z*), aquatic toxicity parameters (LC50 and chronic values, ChV), test organisms (fish or daphnids), exposure durations (96 h for fish acute studies, 48 h for daphnid acute studies, and preferable durations for chronic endpoints), and flags indicating solubility- or log K_{ow}-based considerations. Triclosan displays relatively high toxicity to both fish and daphnids, evidenced by acute LC50 values of 0.965 and 0.701 mg L^{-1}, respectively, and corresponding low chronic thresholds, indicating a heightened hazard potential. By contrast, most identified intermediates (T4a, T4b, T4c, T4d, T4e, T11a, T11b, and T11c) exhibit substantially lower toxicity, with the notable exceptions of T2 and T3. Both T2 and T3 show a "no effects at saturation" flag due to their high log K_{ow}, which indicates that under standard aquatic conditions, their solubility may be too low to reach the concentrations required for acute or chronic effects in water. Consequently, these findings suggest that electrochemical oxidation can mitigate TCS-related ecological risks, as most resultant byproducts pose less harm than the parent compound.

3.6. Assessing the performance and scalability of MnO_2 electrodes in complex environments

The performances of the α- and δ-MnO_2 electrodes were examined in a scaled-up (300 mL) electrolysis of TCS in different environments. The performances of the prepared MnO_2 electrodes were compared with those of other common anodes, such as platinum mesh and BDD electrodes. Titania-CC was also prepared via a hydrothermal method, and its catalytic efficiency was compared with the other electrodes. α- and δ-phase MnO_2 exhibited the greatest catalytic degradation of the five EDCs (Fig. 7a). An adsorption study in an open-circuit setting was also conducted using the MnO_2 electrodes, and the results confirmed that the removal of EDCs was achieved electrochemically (Supplementary Material Fig. S4). Thus, coupled with the results of the TOC analysis, we concluded that EDC degradation was achieved electrocatalytically rather than by surface physisorption. In this study, we also tested the performance of δ-MnO_2 electrodes for degradation of TCS in four different environments (aqueous [Aqs], real wastewater [RWW], synthetic [SL], and real landfill leachates [RL]). The performance of the δ-MnO_2 electrodes was examined in a scaled-up (300 mL) electrolysis of TCS in all of these environments.

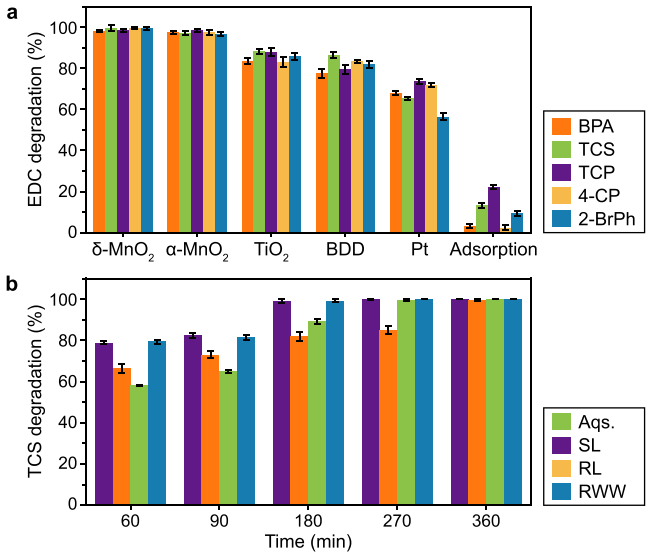

Fig. 7. Comparison of electrocatalytic performances of common electrode and MnO_2-based electrodes for degradation of several endocrine disruptors (EDCs, **a**) and degradation of triclosan (TCS) by δ-MnO_2 electrodes in various environments on a large scale (300 mL) at 80 mA (**b**). BDD: boron-doped diamond; BPA: bisphenol A; TCP: trichlorophenol; 4-CP: 4-chlorophenol; 2-BrPh: 2-bromophenol. Aqs.: aqueous; SL: synthetic leachates; RL: real landfill leachates; RWW: real wastewater on a large scale (300 mL). The average of triplicate data and standard deviation is given in Supplementary Materials Tables S8–S9.

The degradation of organic pollutants present in landfill leachates and industrial wastewater is one of the critical issues in environmental pollution control, as they include many micropollutants and high concentrations of inorganic compounds, thereby hindering the overall degradation process. In this study, we successfully degraded TCS in all possible complex environments (RWW, SL, and RL) and maintained greater than 75% degradation in just 3 h (Fig. 7b). After the degradation reaction was completed in a complex environment (RL and RWW), samples were collected and extracted with DCM and then subjected to GCMS analysis to quantify the leftover TCS in the solution (Supplementary Material Fig. S8).

Fig. 7b shows that TCS was degraded significantly in both simple and complex environments. Compared with the standard aqueous environment (simple environment), the degradation efficiency was slightly lower in the SL and RL environments, but 98% TCS degradation was nevertheless achieved in 6 h, which indicated that the presence of many wastewater species did not influence TCS degradation (Fig. 7b). Moreover, TCS degradation was achieved in real wastewater that was comparable to the TCS degradation in the standard aqueous environment. These results confirm that noble metal catalysts, such as gold or Ag, can be replaced with earth-abundant material-based catalysts (Mn), as the latter exhibit remarkable catalytic performances that approach practical requirements. This opens an avenue for future wastewater remediation and represents significant progress toward closing the anthropogenic carbon cycle to realize global sustainability.

3.7. Environmental implications

Removal of EDCs from wastewater through advanced oxidation processes is currently challenged by the use of toxic oxidants and chemicals to initiate the oxidation reaction, the large amounts of noxious residuals that result from incomplete mineralization, and excessive energy input. Current endeavors to achieve the electrocatalytic mineralization of various EDCs via two highly active MnO_2 phases, α-MnO_2, and δ-MnO_2, were fabricated on a cost-effective CC surface. The resulting MnO_2 catalysts were mostly utilized to accelerate mineralization in real wastewater streams (chlorinated wastewater, real wastewater, and synthetic and real landfill leachates) without the addition of oxidants for ROS generation. Moreover, the performance of the α- and δ-MnO_2 electrodes was also examined in a scaled-up (300 mL) electrolysis of TCS in a synthetic leachate (SL) environment; they maintained 98% TCS degradation, which indicated that the presence of over 10 other common wastewater species did not influence TCS mineralization. Significantly, the MnO_2-CC electrocatalyst performs robustly in real environmental matrices without additional oxidants or chemicals, produces no residual byproducts, and exhibits oxidative performance comparable to that of precious metal catalysts. These favorable features enabled MnO_2-electrocatalyst (Earth-abundant) to be a promising, sustainable, efficient, and scalable solution toward developing catalyst-driven technologies for completely mineralizing multiple organic pollutants.

4. Conclusion

In summary, two highly active MnO_2 phases, α-MnO_2 and δ-MnO_2, were fabricated on a cost-effective CC surface, and the resulting MnO_2 catalysts were comprehensively characterized. The MnO_2 catalysts achieved nearly complete EDC degradation in a pH-neutral chlorinated aqueous environment similar to typical wastewater. α-MnO_2-CC was found to possess unique nanostructures that facilitate the degradation of small aromatic compounds and to contain more Mn^{4+} than Mn^{3+} on its surface, endowing it with enhanced catalytic performance before it reaches the onset potential of the OER. Compared with α-MnO_2, δ-MnO_2 delivered a more stable electrocatalytic performance overall and performed better at high-current flows. These catalytic differences allow the treatment of targeted pollutants, such as mono-aromatic or poly-aromatic organic pollutants. ROS identification by EPR and UV–vis spectroscopy confirmed the presence of various highly reactive intermediates, such as HClO and $O_2^{\bullet-}$. TOC analysis confirmed that aromatic pollutants, such as TCS, were effectively mineralized by the catalysts. Finally, α- and δ-MnO_2 both exhibited good performance in a scaled-up setting and were able to degrade TCS efficiently in an SL environment. By fabricating highly active α-MnO_2 and δ-MnO_2 phases on cost-effective CC surfaces, we developed robust electrocatalysts that efficiently achieve near-complete mineralization of endocrine disruptors in real wastewater streams without additional oxidants, thereby overcoming the challenges of toxic initiators, incomplete mineralization, and high energy inputs associated with traditional advanced oxidation processes. Thus, we have developed an efficient Earth-abundant metal catalyst that exhibits oxidative performance comparable to that of precious metal catalysts.

CRediT authorship contribution statement

Asma Batool: Writing - Review & Editing, Writing - Original Draft, Visualization, Validation, Methodology, Investigation, Formal analysis, Data curation, Conceptualization. **Shan Shao:** Visualization. **Kartick Chandra Majhi:** Visualization. **Azeem Mushtaq:** Visualization. **Yi Jiang:** Writing - Review & Editing, Visualization. **Wingkei Ho:** Writing - Review & Editing, Visualization. **Yiu Fai Tsang:** Writing - Review & Editing, Visualization. **Yuhe He:** Writing - Review & Editing, Visualization. **Kenneth Mei Yee Leung:** Writing - Review & Editing, Visualization. **Jason Chun-Ho Lam:** Writing - Review & Editing, Visualization, Supervision, Investigation, Conceptualization.

Data availability

No data was used for the research described in the article.

Declaration of competing interest

The authors declare that they have no known competing financial interests or personal relationships that could have appeared to influence the work reported in this paper.

Acknowledgement

This work was partially supported by the Innovation and Technology Commission (ITC) of the government of Hong Kong SAR, which provides regular research funding to the State Key Laboratory of Marine Pollution (SKLMP). However, any opinions, findings, conclusions, or recommendations expressed in this publication do not reflect the views of the Government of Hong Kong SAR or the ITC. This work was partially supported by the Environment and Conservation Fund (ECF) of the government of Hong Kong SAR (16/2020). Any opinions, findings, conclusions or recommendations expressed in this material/event do not necessarily reflect the views of the Government of the Hong Kong Special Administrative Region and the Environment and Conservation Fund.

Appendix A. Supplementary data

Supplementary data to this article can be found online at https://doi.org/10.1016/j.ese.2025.100559.

References

[1] A. Batool, S. Valiyaveettil, Sequential removal of oppositely charged multiple compounds from water using surface-modified cellulose, Ind. Eng. Chem. Res. 61 (1) (2021) 716–726.
[2] Y. Liu, X.-J. Luo, L.-Q. Huang, L.-H. Yu, B.-X. Mai, Bioaccumulation of persistent halogenated organic pollutants in insects: common alterations to the pollutant pattern for different insects during metamorphosis, Environ. Sci. Technol. 52 (2018) 5145–5153.
[3] C.C. Viggi, M. Tucci, M. Resitano, S. Crognale, M.L. Di Franca, S. Rossetti, F. Aulenta, Coupling of bioelectrochemical toluene oxidation and trichloroethene reductive dechlorination for single-stage treatment of groundwater containing multiple contaminants, Environ. Sci. Technol. 11 (2022) 100171.
[4] P.D. Jepson, R.J. Law, Persistent pollutants, persistent threats, sci. 352 (2016) 1388–1389.
[5] H. Singer, S. Müller, C. Tixier, L. Pillonel, Triclosan: occurrence and fate of a widely used biocide in the aquatic environment: field measurements in wastewater treatment plants, surface waters, and lake sediments, Environ. Sci. Technol. 36 (2002) 4998–5004.
[6] Z. Luo, Y. He, D. Zhi, L. Luo, Y. Sun, E. Khan, L. Wang, Y. Peng, Y. Zhou, D.C. Tsang, Current progress in treatment techniques of triclosan from wastewater: a review, Sci. Total Environ. 696 (2019) 133990.
[7] C.A. Martínez-Huitle, M. Panizza, Electrochemical oxidation of organic pollutants for wastewater treatment, Curr. Opin. Electrochem. 11 (2018) 62–71.
[8] B. Quan, X. Li, H. Zhang, C. Zhang, Y. Ming, Y. Huang, Y. Xi, X. Weihua, L. Yunguo, Y. Tang, Technology and principle of removing triclosan from aqueous media: a review, Chem. Eng. J. 378 (2019) 122185.
[9] P. Guerra, S. Teslic, A. Shah, A. Albert, S.B. Gewurtz, S.A. Smyth, Occurrence and removal of triclosan in Canadian wastewater systems, Environ. Sci. Pollut. Res. 26 (2019) 31873–31886.
[10] H. Li, Q. Zeng, F. Zan, S. Lin, T. Hao, In situ coagulation-electrochemical oxidation of leachate concentrate: a key role of cathodes, Estud. Sobre Educ. ESE 16 (2023) 100267.
[11] S. Mosquera-Romero, E. Ntagia, D.P. Rousseau, A. Esteve-Núñez, A. Prévoteau, Water treatment and reclamation by implementing electrochemical systems with constructed wetlands, ESE. 16 (2023) 100265.
[12] J. Ding, L. Bu, B. Cui, G. Zhao, Q. Gao, L. Wei, Q. Zhao, D.D. Dionysiou, Assessment of solar-assisted electrooxidation of bisphenol AF and bisphenol A on boron-doped diamond electrodes, Estud. Sobre Educ. ESE 3 (2020) 100036.
[13] H. Wang, S. Xue, W. Wang, F. Gao, S. Yi, J. Li, Y. Yang, E. Zhao, J. Wang, J. Wang, CNTs/Ce co-doped PbO2 anode for electro-oxidation of triclosan: fabrication, kinetics, and degradation mechanism based on DFT calculations, J. Water Proc.engineering. 64 (2024) 105748.
[14] Z. Song, N. Wang, L. Zhu, A. Huang, X. Zhao, H. Tang, Efficient oxidative degradation of triclosan by using an enhanced Fenton-like process, J. Chem. Eng. 198 (2012) 379–387.
[15] M. Munoz, Z.M. De Pedro, J.A. Casas, J.J. Rodriguez, Triclosan breakdown by Fenton-like oxidation, Chem. Eng. J. 198 (2012) 275–281.
[16] Y. Guo, X. Zhang, D. Zhang, S. Li, H. Wang, Y. Peng, Z. Bian, Catalysts containing Fe and Mn from dewatered sludge showing enhanced electrocatalytic degradation of triclosan, Environ. Res. 214 (2022) 114065.
[17] C. Magro, E.P. Mateus, J.M. Paz-Garcia, A.B. Ribeiro, Emerging organic contaminants in wastewater: understanding electrochemical reactors for triclosan and its by-products degradation, Chemosphere 247 (2020) 125758, https://doi.org/10.1016/j.chemosphere.2019.125758.
[18] D. Maharana, J. Niu, N.N. Rao, Z. Xu, J. Shi, Electrochemical degradation of triclosan at a Ti/SnO2-Sb/Ce-PbO2 anode, Clean - Soil Air Water 43 (2015) 958–966, https://doi.org/10.1002/clen.201400180. (Accessed 7 November 2023).
[19] C. Zhou, Y. Wang, S. Tang, Y. Wang, H. Yu, J. Niu, Insights into the electrochemical degradation of triclosan from human urine: kinetics, mechanism and toxicity, Chemosphere 264 (2021) 128598, https://doi.org/10.1016/j.chemosphere.2020.128598.
[20] N. Stamatis, M. Antonopoulou, D. Hela, I. Konstantinou, Photocatalytic degradation kinetics and mechanisms of antibacterial triclosan in aqueous TiO2 suspensions under simulated solar irradiation, J. Chem. Technol. Biotechnol. 89 (2014) 1145–1154, https://doi.org/10.1002/jctb.4387. (Accessed 7 November 2023).
[21] M. Munoz, Z.M. de Pedro, J.A. Casas, J.J. Rodriguez, Triclosan breakdown by Fenton-like oxidation, Chem. Eng. J. 198–199 (2012) 275–281, https://doi.org/10.1016/j.cej.2012.05.097.
[22] X. Zhou, D. Xu, Y. Chen, Y. Hu, Enhanced degradation of triclosan in heterogeneous E-Fenton process with MOF-derived hierarchical Mn/Fe@PC modified cathode, J. Chem. Eng. 384 (2020) 123324, https://doi.org/10.1016/j.cej.2019.123324.
[23] Z. Song, N. Wang, L. Zhu, A. Huang, X. Zhao, H. Tang, Efficient oxidative degradation of triclosan by using an enhanced Fenton-like process, Chem. Eng. J. 198–199 (2012) 379–387, https://doi.org/10.1016/j.cej.2012.05.067.
[24] V. Bokare, K. Murugesan, Y.-M. Kim, J.-R. Jeon, E.-J. Kim, Y.S. Chang, Degradation of triclosan by an integrated nano-bio redox process, Bioresour. Technol. 101 (2010) 6354–6360, https://doi.org/10.1016/j.biortech.2010.03.062.
[25] K. Lin, W. Liu, J. Gan, Oxidative removal of bisphenol A by manganese dioxide: efficacy, products, and pathways, Environ. Sci. Technol. 43 (2009) 3860–3864.
[26] X. Lu, T. Zhai, X. Zhang, Y. Shen, L. Yuan, B. Hu, L. Gong, J. Chen, Y. Gao, J. Zhou, WO3–x@ Au@ MnO2 core–shell nanowires on carbon fabric for high-performance flexible supercapacitors, J. Adv. Mater. 24 (2012) 938–944.
[27] S. Taujale, L.R. Baratta, J. Huang, H. Zhang, Interactions in ternary mixtures of MnO2, Al2O3, and natural organic matter (NOM) and the impact on MnO2 oxidative reactivity, Environ. Sci. Technol. 50 (2016) 2345–2353.
[28] H. Zhang, C.-H. Huang, Oxidative transformation of triclosan and chlorophene by manganese oxides, Environ. Sci. Technol. 37 (2003) 2421–2430.
[29] S. Laha, R.G. Luthy, Oxidation of aniline and other primary aromatic amines by manganese dioxide, Environ. Sci. Technol. 24 (1990) 363–373.
[30] H. Zhang, C.-H. Huang, Oxidative transformation of fluoroquinolone antibacterial agents and structurally related amines by manganese oxide, Environ. Sci. Technol. 39 (2005) 4474–4483.
[31] H. Zhang, C.-H. Huang, Reactivity and transformation of antibacterial N-oxides in the presence of manganese oxide, Environ. Sci. Technol. 39 (2005) 593–601.
[32] Y. Meng, W. Song, H. Huang, Z. Ren, S.-Y. Chen, S.L. Suib, Structure–property relationship of bifunctional MnO2 nanostructures: highly efficient, ultrastable electrochemical water oxidation and oxygen reduction reaction catalysts identified in alkaline media, J. Am. Chem. Soc. 136 (2014) 11452–11464.
[33] J.N. Apell, S. Kliegman, C. Sola-Gutierrez, K. McNeill, Linking Triclosan's structural features to its environmental fate and photoproducts, Environ. Sci. Technol. 54 (2020) 14432–14441, https://doi.org/10.1021/acs.est.0c05121.
[34] M. Pernetti, L.D. Palma, Experimental evaluation of inhibition effects of saline wastewater on activated sludge, Environ. Technol. 26 (2005) 695–704.
[35] C.C. McCrory, S. Jung, J.C. Peters, T.F. Jaramillo, Benchmarking heterogeneous electrocatalysts for the oxygen evolution reaction, J. Am. Chem. Soc. 135 (2013) 16977–16987.
[36] T. Yu, H. Liu, M. Huang, J. Zhang, D. Su, Z. Tang, J. Xie, Y. Liu, A. Yuan, Q. Kong, Zn 2 GeO 4 nanorods grown on carbon cloth as high performance flexible lithium-ion battery anodes, RSC Adv. 7 (2017) 51807–51813.
[37] X. Long, L. Tian, J. Wang, L. Zhang, Y. Chen, A. Emin, X. Wang, W. Xie, D. Liu, Y. Fu, Interconnected δ-MnO2 nanosheets anchored on activated carbon cloth as flexible electrode for high-performance aqueous asymmetric supercapacitors, J. Electroanal. Chem. 877 (2020) 114656.
[38] N. Sinan, Ünür Yılmaz, E. PEDOT, PSS enhanced electrochemical capacitive performance of graphene-templated delta-MnO2, J. Electrochem. Sci. Technol. (2020) 50–59.
[39] D. Chinnadurai, M. Nallal, H.-J. Kim, O.L. Li, K.H. Park, K. Prabakar, Mn3+ active surface site enriched manganese phosphate nano-polyhedrons for enhanced bifunctional oxygen electrocatalyst, ChemCatChem 12 (2020) 2348–2355, https://doi.org/10.1002/cctc.202000164.
[40] F. Bai, Y. He, L. Xu, Y. Wang, Y. Wang, Z. Hao, F. Li, Improved ORR/OER bifunctional catalytic performance of amorphous manganese oxides prepared by photochemical metal–organic deposition, RSC Adv. 12 (2022) 2408–2415,

https://doi.org/10.1039/D1RA08618A, 10.1039/D1RA08618A.
[41] J. Suntivich, H.A. Gasteiger, N. Yabuuchi, H. Nakanishi, J.B. Goodenough, Y. Shao-Horn, Design principles for oxygen-reduction activity on perovskite oxide catalysts for fuel cells and metal–air batteries, Nat. Chem. 3 (2011) 546–550, https://doi.org/10.1038/nchem.1069.
[42] J. Rossmeisl, Z.W. Qu, H. Zhu, G.J. Kroes, J.K. Nørskov, Electrolysis of water on oxide surfaces, J. Electroanal. Chem. 607 (2007) 83–89, https://doi.org/10.1016/j.jelechem.2006.11.008.
[43] K. Li, C. Chen, H. Zhang, X. Hu, T. Sun, J. Jia, Effects of phase structure of MnO2 and morphology of δ-MnO2 on toluene catalytic oxidation, Appl. Surf. Sci. 496 (2019) 143662, https://doi.org/10.1016/j.apsusc.2019.143662.
[44] Y. Zhou, Z. Zhou, L. Hu, R. Tian, Y. Wang, H. Arandiyan, F. Chen, M. Li, T. Wan, Z. Han, et al., A facile approach to tailor electrocatalytic properties of MnO2 through tuning phase transition, surface morphology and band structure, J. Chem. Eng. 438 (2022) 135561, https://doi.org/10.1016/j.cej.2022.135561.
[45] X. Zheng, L. Yu, B. Lan, G. Cheng, T. Lin, B. He, W. Ye, M. Sun, F. Ye, Three-dimensional radial α-MnO2 synthesized from different redox potential for bifunctional oxygen electrocatalytic activities, J. Power Sources 362 (2017) 332–341, https://doi.org/10.1016/j.jpowsour.2017.07.027.
[46] S. Chen, M. Li, Q. Ji, T. Feng, S. Lan, K. Yao, Effect of the chloride ion on advanced oxidation processes catalyzed by Fe-based metallic glass for wastewater treatment, JMR&T 117 (2022) 49–58.
[47] R.C. Ropp, Chapter 2 - group 17 (H, F, Cl, Br, I) alkaline earth compounds, in: R.C. Ropp (Ed.), Encyclopedia of the Alkaline Earth Compounds, Elsevier, 2013, pp. 25–104.
[48] D. Zehavi, J. Rabani, Oxidation of aqueous bromide ions by hydroxyl radicals. Pulse radiolytic investigation, J. Phys. Chem. 76 (1972) 312–319, https://doi.org/10.1021/j100647a006.
[49] B.M. Matthew, C. Anastasio, A chemical probe technique for the determination of reactive halogen species in aqueous solution: Part 1 – bromide solutions, Atmos. Chem. Phys. 6 (2006) 2423–2437, https://doi.org/10.5194/acp-6-2423-2006.
[50] K.M. Macounová, N. Simic, E. Ahlberg, P. Krtil, Electrochemical water-splitting based on hypochlorite oxidation, J. Am. Chem. Soc. 137 (2015) 7262–7265, https://doi.org/10.1021/jacs.5b02087.
[51] B. Matthew, C. Anastasio, A chemical probe technique for the determination of reactive halogen species in aqueous solution: Part 1–bromide solutions, Atmos. Chem. Phys. 6 (2006) 2423–2437.
[52] F.A. Villamena, Y. Liu, J.L. Zweier, Superoxide radical anion adduct of 5,5-Dimethyl-1-pyrroline N-oxide. 4. Conformational effects on the EPR hyperfine splitting constants, J. Phys. Chem. A 112 (2008) 12607–12615, https://doi.org/10.1021/jp8070579.
[53] F.A. Villamena, A. Rockenbauer, J. Gallucci, M. Velayutham, C.M. Hadad, J.L. Zweier, Spin trapping by 5-carbamoyl-5-methyl-1-pyrroline N-oxide (AMPO): theoretical and experimental studies, J. Org. Chem. 69 (2004) 7994–8004.
[54] S.-Y. Liou, M.C. Dodd, Evaluation of hydroxyl radical and reactive chlorine species generation from the superoxide/hypochlorous acid reaction as the basis for a novel advanced oxidation process, Water Res. 200 (2021) 117142, https://doi.org/10.1016/j.watres.2021.117142.
[55] G.S. Dhillon, S. Kaur, R. Pulicharla, S.K. Brar, M. Cledón, M. Verma, R.Y. Surampalli, Triclosan: current status, occurrence, environmental risks and bioaccumulation potential, Int. J. Environ. Res. Publ. Health 12 (2015) 5657–5684.
[56] S. Schröder, M.-F. San-Román, I. Ortiz, Photocatalytic transformation of triclosan. Reaction products and kinetics, Catalysts 10 (2020) 1468.